Front. Energy 2025, 19(3): 312–325
https://doi.org/10.1007/s11708-025-0984-6

RESEARCH ARTICLE

Performance analysis of a novel unassisted photoelectrochemical water splitting hybrid system based on spectral beam splitting

Baoyuan Wang, Suyi Yang, Tuo Zhang, Yukai Liu, Sheng Yang, Luning Li, Weiding Wang, Jinzhan Su (✉)

International Research Center for Renewable Energy, State Key Laboratory of Multiphase Flow in Power Engineering, Xi'an Jiaotong University, Xi'an 710049, China

Abstract Photoelectrochemical (PEC) water splitting, particularly self-biased PEC systems, holds great promise for solar energy utilization. However, the limited transparency of most photoelectrodes presents challenges in fabricating tandem photoelectrodes with photovoltaic (PV) cells for self-biased water splitting. Herein, a novel self-biased hybrid system integrating photoelectrodes (TiO_2, $BiVO_4$), beam splitters (BSs), and PV cell was proposed to enhance solar energy utilization and PEC water splitting performance. The results indicate that the integration of BSs significantly improves the current densities of both self-biased PV-PEC systems and single PEC systems. The current density of self-biased water splitting system with BSs exceeds that of the conventional TiO_2 + BVO-PV system, and the intersection point of the *I–V* curves for the photoanodes and solar cell is closer to the maximum power output of the solar cell. The effective utilization of the solar spectrum by both the photoelectrode and the PV cell in the hybrid system with BSs significantly increases the power output by a factor of 18.8 compared to the conventional tandem self-biased system. The predicted results indicate that the hydrogen production rate of the system with BSs is 12.1 μmol/(h·cm^2), while the STH efficiency is enhanced by a factor of 12.38 and 19.87 compared to conventional TiO_2 + BVO-PV and TiO_2/BVO-PV tandem PV-PEC systems, respectively, demonstrating the advantage of the water splitting system with spectral BSs. In conclusion, this work provides an innovative approach of achieving self-biased water splitting by coupling spectral BSs with a PV-PEC system, resulting in improved solar energy harvesting efficiency.

Keywords spectral beam splitter, photovoltaic-photoelectrochemical (PV-PEC), water splitting, spectrum, energy flow

1 Introduction

Solar-driven photoelectrochemical (PEC) water splitting is one of the most promising and cost-effective methods for solar energy utilization, which plays a crucial role in mitigating carbon emissions and environmental remediation [1]. Current research in PEC water splitting focuses on enhancing the efficiency, stability, and scalability of the process. This includes developing photoelectrodes with efficient surface catalytic activity [2,3], improving sunlight utilization efficiency [4,5], exploring multi-physical fields within the electrode [6,7], and optimizing reactor system designs [8,9]. However, PEC water splitting suffers from low efficiency and the need for additional voltage bias. A hybrid system combining PV technology (for efficient solar-to-electricity conversion) with PEC (for direct water splitting) can achieve higher overall energy conversion efficiencies compared to standalone technologies. Spectral splitting strategies can further enhance performance by directing specific parts of the spectrum to the PV and PEC components [10].

Currently, there are two primary configurations for the self-biased water splitting systems. One configuration is the tandem PEC model (Model T) [11,12], which employs either a prepositional semitransparent photoelectrode/PV cell or a postpositional PV cell/photoelectrode arrangement to achieve full spectrum solar energy

Received Oct. 26, 2024; accepted Dec. 25, 2024; online Feb. 15, 2025
Correspondence: Jinzhan Su, j.su@mail.xjtu.edu.cn

utilization. The other configuration is the parallel arrangement model (Model P) [13,14], where both the photoelectrode and the PV cell are exposed to the entire solar spectrum.

Compared to Model P, Model T offers the advantage optimizing light absorption across different spectral regions by integrating two or more absorbers with different light absorption ranges. In the T configuration, when the PV cell is positioned in front of the photoelectrode, it achieves a higher photoelectric conversion efficiency (PCE). However, this configuration reduces the photoanode's efficiency due to overlapping light absorption. Alternatively, positioning the photoelectrode upfront necessitates a highly transparent design to minimize scattering and ensure efficient light transmission to the rear PV cell.

In Mode T, metal oxide semiconductors such as TiO_2 [15–17], WO_3 [18,19], $BiVO_4$ [20,21], and Fe_2O_3 [22,23] have been extensively studied and used for the pre-photoanode, because of their good light transmittance. Narrow bandgap semiconductors, such as silicon or perovskite materials, are typically used for the postpositional photocathode or PV cell [24,25].

Spectral splitting has emerged as a promising approach for efficient solar energy utilization [26,27]. The basic principle of spectral splitting involves reflecting or transmitting different parts of the solar spectrum to different light absorbers, such as photoelectrode [28], PV cells [29], thermoelectrics [30], and others [31], using optical coatings [32,33] or fluid-based filters [34,35]. This approach has been successfully applied in PV, thermoelectric, and photothermal catalysis systems, demonstrating its potential to enhance overall efficiency.

For instance, Lu et al. [36] developed a system leveraging spectral beam splitting and serial thermal circuits, achieving a comprehensive efficiency improvement of 17.9% by increasing the outlet water temperature by 3.9 °C and decreasing the solar cell temperature by 9.4 °C. Kandil et al. [37] conducted an experimental and theoretical study of a hybrid/thermoelectric generator system incorporating a beam splitter (BS), achieving efficiencies of up to 20% and 3% for visible light conversion and thermal energy conversion, respectively. Wu et al. [38] proposed a novel cascading solar cell design with a concentrating spectral splitting system, achieving an electrical efficiency of 35.69% under 1000-sun concentration, surpassing conventional single PV systems by 9.55%. Additionally, Hogerwaard et al. [39] designed and evaluated an integrated solar concentration system with spectrum splitting to power both PEC hydrogen production and PV electricity generation. The performance of key components such as the concentrator, spectrum-splitting mirror, electrolyzer, PEC reactor, and PV module, was experimentally analyzed under direct sunlight conditions.

It has been proved that spectral BSs are feasible for solar energy conversion and utilization. However, there is limited research on the application of BSs in self-biased PEC water splitting systems or on the experimental investigation of energy flow in such hybrid PV-PEC water splitting systems. In addition, the use of spectral BSs makes it possible to utilize the whole solar spectrum in the Model T PEC water splitting configuration by directing specific parts of the spectrum of incident light to the photoelectrode surface.

In this study, a novel integrated system is developed, comprising a series of spectral BSs, photoelectrodes, and PV cells. This system couples spectral beam splitting with self-biased PEC water splitting, showing enhanced efficiency in both the PEC and PV processes compared to traditional Model T configurations. Experimental investigations focus on assessing the impact of spectral splitting on PV cells and photoelectrodes, quantifying absorption losses due to BSs, photoelectrodes, and PV cells, and analyzing energy flow processes. The efficiencies of individual components are calculated and compared across three distinct system architectures.

2 System overview

2.1 Photoelectrode and characterization

Preparation of the photoelectrodes: The TiO_2 used in this study was prepared following a method described in a recent study, where acetylacetone, tetrabutyl titanate ($Ti(OBu)_4$), and anhydrous ethanol were used as precursors to grow a TiO_2 nanorod film [40]. The $BiVO_4$ photoanode was prepared using the metal-organic decomposition (MOD) method [41], with a few modifications made to achieve a uniform, worm-like $BiVO_4$ photoanode, as shown in Fig. S1 (see Electronic Supplementary Material).

An aqueous solution of 0.5 mol/L Na_2SO_4 was used as the electrolyte for the electrochemical measurements, with the pH of the solution being measured using a pH meter (PHS-3E). PEC measurements were conducted using a computer-controlled electrochemical workstation (CHI 760D) with a three-electrode setup: the TiO_2 and $BiVO_4$ samples served as the working electrode, a platinum plate was used as the counter electrode, and an Ag/AgCl electrode (4 mol/L KCl) acted as the reference electrode. The morphological and crystallographic characterization of the samples is described in detail in the Electronic Supplementary Material. UV-vis absorption spectra of the photoelectrodes were tested using a UV-7000 spectrophotometer with the light incident at an angle of 90°.

2.2 BS

The BS is used to divide the incident light into two beams

with different spectral ranges for separate utilization. The shorter wavelength light is reflected by the BS, while the longer wavelength light is transmitted, achieving spectral separation. When the BS is placed at a 45° angle in the optical path, the reflected shorter-wavelength light is directed toward the photoanode. Given the different absorption spectra of different photoelectrodes, spectral BSs with different reflection and transmission spectral ranges are employed for each photoanode, as shown in Fig. S2.

As depicted in Fig. 1, the BSs exhibit high spectral separation efficiency, with both reflectance and transmittance approaching 100% at specific incident angles. The photoelectric conversion efficiency of the PV cell used in the experiments within the wavelength range of 300–800 nm is shown in Fig. S3. The results indicate that the PV achieves higher conversion efficiency between 480 and 800 nm compared to the 300 and 480 nm range. Therefore, by transmitting the 480–800 nm spectral range to the PV and reflecting the other spectral range to the photoanode, an overall higher efficiency can be achieved.

2.3 System description and experimental setup

A novel cascaded solar water splitting system utilizing BSs has been developed, as schematically illustrated in Fig. 2. The system mainly consists of a BS subsystem, a PEC subsystem, and a PV cell. The PEC subsystem employs TiO_2 and $BiVO_4$ as photoanodes. The specifications of the components are listed in Table S1.

As shown in Fig. 2, the incident simulated sunlight is first divided into two parts by BS1. The shorter wavelength portion is reflected onto the TiO_2 photoanode surface, while the remaining longer wavelength portion is transmitted to BS2. The light passing through BS2 is further divided into two parts: the shorter wavelength light is reflected to the $BiVO_4$ photoanode, while the longer wavelength light is transmitted to illuminate on the PV cell, which converts this light into electrical energy and serves as the bias voltage source for the PEC cell.

In this process, the simulated sunlight with different wavelength ranges is directed to different absorbers. This approach is similar to the principle of the traditional Model T water splitting system. However, the conventional tandem system suffers from significant light loss due to the poor transparency of the front absorber photoanode and strong diffuse reflection, which results in reduced light intensity transmitted to the rear light absorber. In contrast, the hybrid system developed in this study significantly minimizes light loss. The high

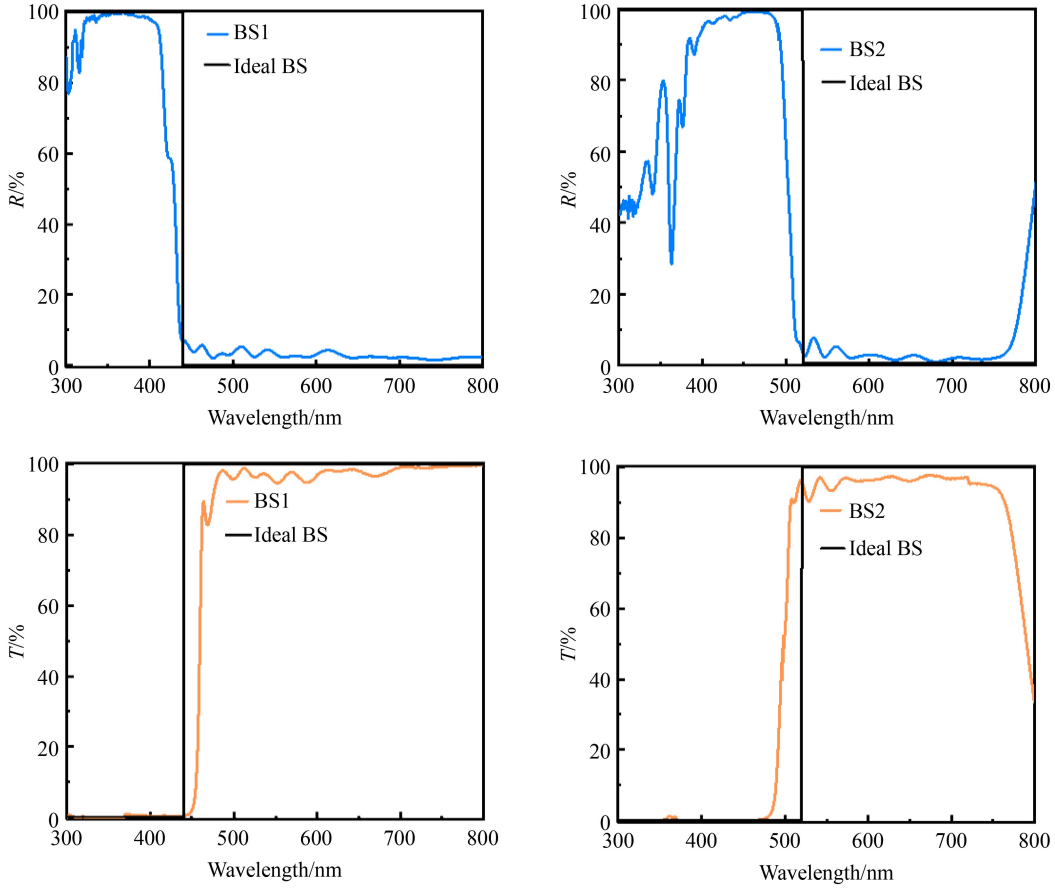

Fig. 1 Measured reflectance and transmittance of BSs, where the incident angle is 45°.

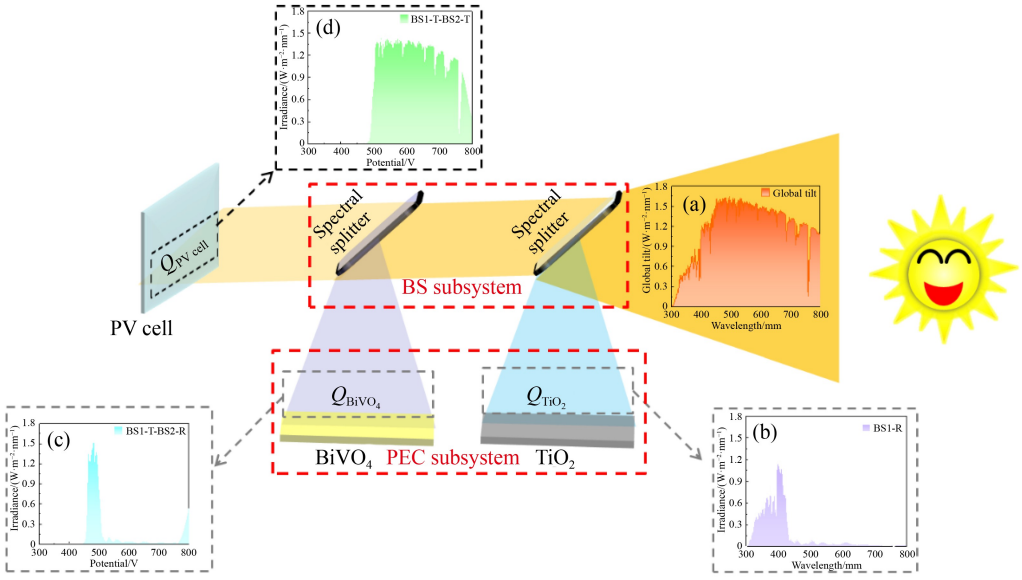

Fig. 2 Schematic diagram of PV-PEC water splitting based on BSs.
(a) Spectrum reaching the BS1; (b) spectrum reaching the TiO_2; (c) spectrum reaching the $BiVO_4$; (d) spectrum reaching the PV cell.

reflectance and transmittance of the spectral BSs ensures that the rear absorber receives more incident light.

The configuration of the PV-PEC hybrid water splitting system developed in this study is shown in Fig. S4. To minimize light divergence loss between various components, the distance between the two BSs and the solar cell is kept to less than 1.5 cm. Additionally, the two BSs and the solar cell are positioned on the same horizontal plane. The area of the BSs is larger than that of the photoanode and the solar cell, ensuring that the entire surfaces of both the photoanode and solar cell are fully illuminated by the simulated sunlight.

2.4 Analysis

The calculations for analysis are performed using the Engineering Equation Solver (EES). The points in the system are defined as follows: the location preceding spectral BS1 is designated as state point 1. After reflection from BS1 onto the TiO_2 surface, it becomes state point 2. When the light transmits through BS1 to the surface of BS2, it is regarded as state point 3. Subsequently, reflection from BS2 onto the $BiVO_4$ surface leads to state point 4, and further transmission through BS2 onto the PV module results in state point 5, as illustrated in Fig. 3.

To analyze and quantify the energy flow at each state point, the following primary assumptions were made:

• Only solar spectra with wavelengths between 300 and 800 nm are considered.

• The angles of the two spectral BSs, relative to the light path, are fixed as a constant, 45°.

• The loss of light beam in air and electrolyte over short distance is neglected during the measurements.

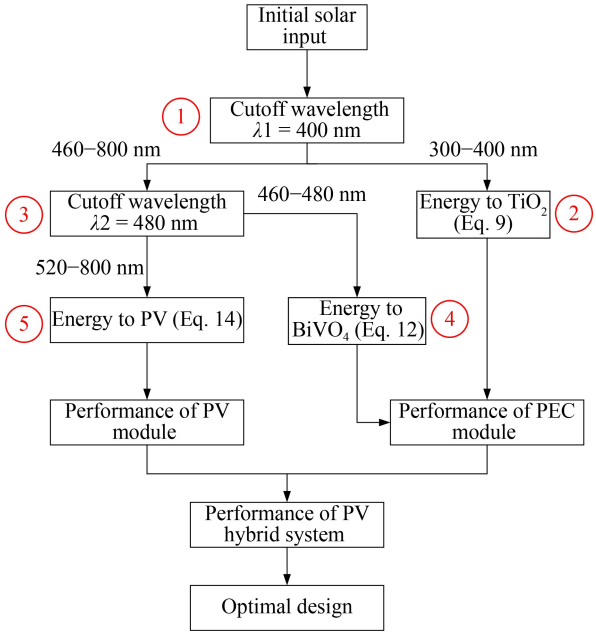

Fig. 3 Flowchart of optimal design for PV-PEC hybrid system.

• The effective area of each BS is 2.25 cm^2, and they are positioned at the same height.

• The area of the incident solar light is larger than that of the BSs.

The efficiency (η_{PV}) of the PV cell is calculated based on the maximum power output and the incident solar energy, as expressed by

$$\eta_{PV} = \frac{V_{OC} \times I_{SC} \times FF}{A \times P_{light}}, \quad (1)$$

where V_{OC} and I_{SC} are the open circuit voltage and short

circuit current of the PV module, respectively; *FF* is the fill factor, which is calculated as follows, *A* is the area of the PV cell, and P_{light} is the incident light irradiance of AM 1.5 G, which is considered as 1000 W/m^2 in our system.

The *FF* is defined as the ratio of the maximum power output (P_{mpp}) to the value of I_{SC} and V_{OC}.

$$FF = \frac{P_{\text{mpp}}}{I_{\text{SC}} \times V_{\text{OC}}} = \frac{I_{\text{mpp}} \times V_{\text{mpp}}}{I_{\text{SC}} \times V_{\text{OC}}} \times 100\%, \tag{2}$$

where I_{mpp} and V_{mpp} are the current and voltage at the maximum power output, respectively.

The energy of photons is related to their wavelength, as described by Eq. (3)

$$E = \frac{hc}{\lambda}, \tag{3}$$

where *h* is the Planck's constant, *c* is the speed of light, and λ is the wavelength.

To obtain the spectral irradiance, Eq. (4) is used.

$$I_\lambda = E\dot{N}''_{ph,\lambda}, \tag{4}$$

where $\dot{N}''_{ph,\lambda}$ is the flux of photons per unit area and per second. With Eq. (4), it is possible to determine the irradiance of the photons with wavelength in each nm.

$$I = \int I_\lambda \mathrm{d}\lambda. \tag{5}$$

The total energy that reach the system can be generally written as

$$E = A \int I_\lambda \mathrm{d}\lambda. \tag{6}$$

The incident energy to the PV-PEC system is written for the wavelength range of 300–800 nm as

$$E = A_{\text{light}} \int_{300}^{800} I_\lambda \mathrm{d}\lambda, \tag{7}$$

where A_{light} is the illuminated area of the system, which is also the effective area of the spectral BS. Therefore, the energy reaching point 1 could be determined as

$$E_1 = A_{\text{BS1}} \int_{300}^{800} I_{\lambda,1} \mathrm{d}\lambda. \tag{8}$$

The light in the 300–400 nm range is reflected onto the TiO_2 photoanode, and the amount of light energy reaching point 2 can be stated as

$$Q_{\text{TiO}_2} = E_2 = A_{\text{TiO}_2} \int_{300}^{400} I_{\lambda,2} R_{\lambda,1} \mathrm{d}\lambda. \tag{9}$$

where A_{TiO_2} is the exposed area of TiO_2 photoanode, and $R_{\lambda,1}$ is the reflectance of the BS1, which is higher than 95% on average.

The light energy splitting efficiency from solar to point 2 of the BS1 can be written as

$$\eta_{1-2} = \frac{E_2}{E_1}. \tag{10}$$

The BS1 transmits the 460–800 nm spectrum to the next spectral BS2. Therefore, the light energy reaching point 3 can be stated as

$$E_3 = A_{\text{BS2}} \int_{460}^{800} I_{\lambda,3} T_{\lambda,1} \mathrm{d}\lambda, \tag{11}$$

where A_{BS2} is the area of the BS2, and $T_{\lambda,1}$ is the transmittance of the BS1, which is also higher than 95% on average.

The BS2 reflects the light in the 460–480 nm range onto the surface of $BiVO_4$ photoanode as point 4, where the light energy can be calculated as

$$Q_{\text{BiVO}_4} = E_4 = A_{\text{BiVO4}} \int_{460}^{480} I_{\lambda,4} T_{\lambda,1} R_{\lambda,2} \mathrm{d}\lambda, \tag{12}$$

where A_{BiVO_4} is the exposed area of the $BiVO_4$ photoanode, and $R_{\lambda,2}$ is the reflectance of BS2, which is also higher than 95% on average.

In this case, the light energy splitting efficiency of BS2 from point 3 to point 4 of $BiVO_4$ photoanode can be defined as

$$\eta_{3-4} = \frac{E_4}{E_3}. \tag{13}$$

The remaining portion of the light spectrum transmits through BS2 and reaches the surface of the solar cell as point 5. The light energy at this point can be defined as

$$Q_{\text{PV,cell}} = E_5 = A_{\text{Si}} \int_{520}^{800} I_{\lambda,3} T_{\lambda,1} T_{\lambda,2} \mathrm{d}\lambda, \tag{14}$$

where A_{Si} is the illuminated area of the PV cell, and $T_{\lambda,2}$ is the transmittance of BS2, which is also higher than 95% on average.

The efficiency of incident light to electricity of the PV module is expressed as

$$\eta_5 = \frac{I_5 V_5}{E_5} = \frac{FF \times I_{\text{SC},5} \times V_{\text{OC},5}}{E_5} \tag{15}$$

In the hybrid system with BSs, solar energy is the sole form of energy input. Consequently, hydrogen production can be calculated using the solar-to-hydrogen (STH) conversion efficiency, defined as

$$\eta_{\text{STH}} = \frac{V_{\text{H}_2} \times \Delta G}{P_{\text{light}} \times A}, \tag{16}$$

where ΔG is the Gibbs free energy of per mole hydrogen production, which is considered to be 237 kJ/mol at 25 °C; and V_{H_2} is the rate of hydrogen production.

The STH efficiency can be calculated using Eq. (16) based on direct measurement of hydrogen production. Additionally, it can be determined from the photocurrent density generated by the photoelectrode and the Faraday efficiency, calculated as

$$\eta_{\text{STH}} = \frac{J_{\text{op}} \times V_{\text{ref}} \times \eta_{\text{F}}}{P_{\text{light}}}, \tag{17}$$

where J_{op} is the operating photocurrent density of the system, V_{ref} is theoretical voltage of water splitting, which is 1.23 V at 25 °C, and η_{F} is the Faraday

efficiency, which is considered as 100%.

The measurements of PV cell, photoanodes with or without BSs, and the self-biased water splitting systems are shown in Fig. 4, and the energy flow of those systems are calculated according to Eqs. S4–S14. In the structures, the green line indicates the connection between the working electrode of the workstation and the photoanodes or the anode of the PV cell, while the black line shows the connection between the cathode of the PV cell and the photoanode.

3 Results and discussion

3.1 Characterization of photoelectrodes

Figure 5 depicts the surface and cross-sectional scanning electron microscopy (SEM) images of the three photoanode materials used in this study: TiO_2, $BiVO_4$, and $BiVO_4$ spin-coated TiO_2 photoanode (TiO_2/$BiVO_4$). The TiO_2 film exhibits a nanorod array structure, with an average nanorod length of 1.3 μm. In contrast, the $BiVO_4$ film has a relatively dense structure with an average thickness of 0.4 μm. Figures 5(c) and 5(f) illustrate the synthesized TiO_2/$BiVO_4$ composite photoanode, which has an average thickness of approximately 1.8 μm.

To assess the stability of the photoanodes, SEM images of the photoelectrodes after exposure to 1 sun illumination were also taken. The surface morphology of $BiVO_4$ and TiO_2 after electrochemical measurements is shown in Fig. S5.

To gain deeper insights into the structure of the TiO_2/$BiVO_4$ bilayer composite electrode, energy-dispersive X-ray spectroscopy (EDX) and X-ray diffraction (XRD) were conducted to investigate the elemental distribution and crystal structure of the composite. The EDX elemental mapping, shown in Figs. S6 and S7 reveals that Bi and V elements are primarily distributed in the upper layer, while the Ti element concentrates primarily in the lower layer, with the Sn element originating from the fluorine-doped tin oxide-coated glass (FTO) substrate at the base. This result confirms the synthesis of a TiO_2/$BiVO_4$ bilayer composite electrode. The XRD pattern further confirms this by showing characteristic peaks of both TiO_2 (PDF# 00-021-1276) and $BiVO_4$ (PDF# 14-0688) for the TiO_2/$BiVO_4$ photoanode.

3.2 Performance of different configuration of photoelectrodes

3.2.1 Performance of photoelectrode with spectral BSs

To assess the impact of the spectral BSs on the performance of photoanode, the photocurrent density of TiO_2 and $BiVO_4$ was compared under different configurations, as shown in Fig. 4. The results in Fig. S8 show that there is virtually no difference between the two configurations. The values were measured to be 1.33 and 1.25 mA/cm^2 at 1.23 V versus RHE, corresponding to the photocurrent density of the BS1-TiO_2||BS2-$BiVO_4$ system and the sum of the photocurrent densities of TiO_2 with BS1 (BS1-TiO_2) and $BiVO_4$ with BS2 (BS2-$BiVO_4$), measured individually (BS1-TiO_2(1) + BS2-$BiVO_4$(2)), respectively.

Furthermore, the photocurrent densities of BS1-TiO_2

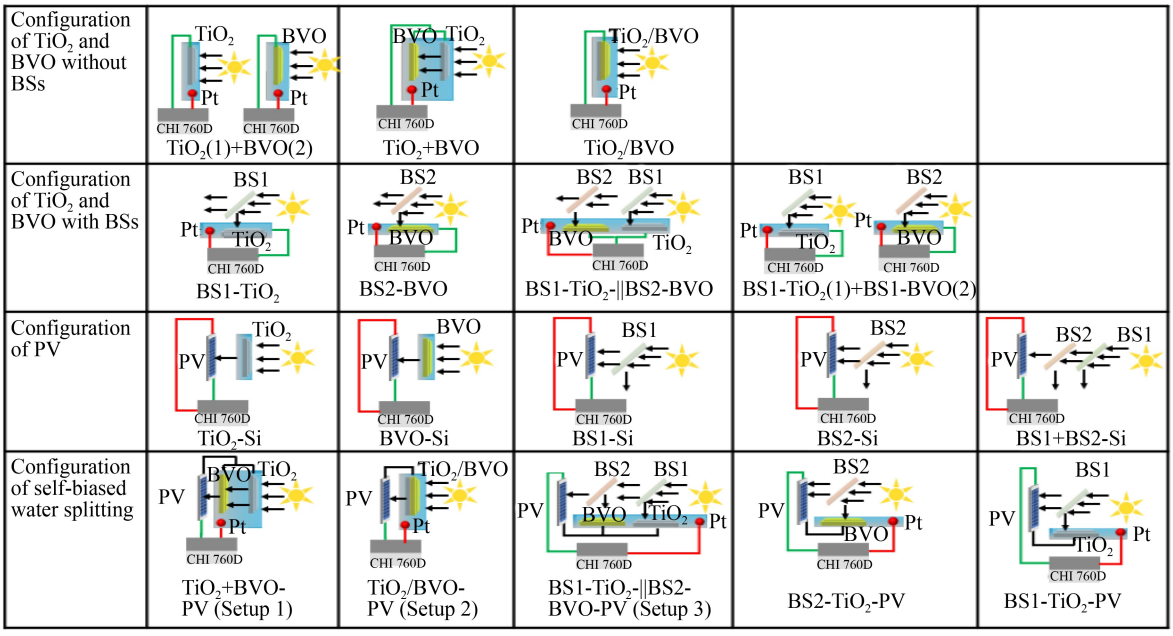

Fig. 4 Measurements of the PV cell, TiO_2, and $BiVO_4$ with and without BSs, as well as the self-biased water splitting systems.

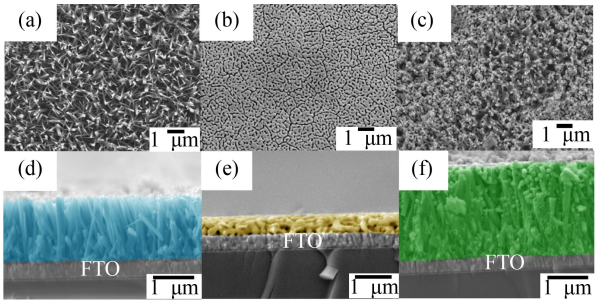

Fig. 5 Top-view and cross-sectional SEM images. (a,d) TiO_2; (b,e) $BiVO_4$; (c,f) TiO_2/$BiVO_4$ photoanodes.

and BS2-$BiVO_4$ were measured separately, as depicted in Fig. 6. The photocurrent densities for BS2-$BiVO_4$ and BS1-TiO_2 were found to be 0.96 and 0.35 mA/cm^2 at 1.23 V versus RHE, respectively. Notably, the photocurrent density of the BS1-TiO_2||BS2-$BiVO_4$ system is about 1.38 and 3.94 times than that of the BS2-$BiVO_4$ and BS1-TiO_2 system, respectively.

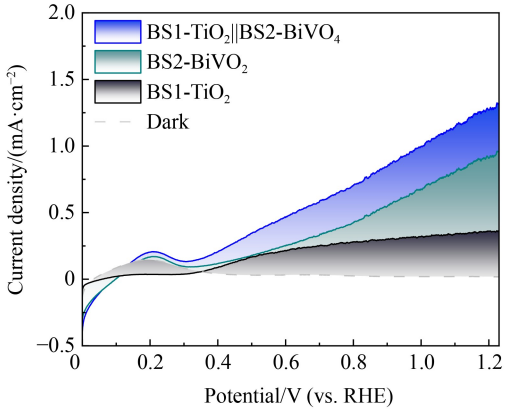

Fig. 6 Photocurrent density of TiO_2 and $BiVO_4$ with different BSs in a typical three-electrode system.

To further confirm that BSs with appropriate spectral ranges do not negatively affect the photocurrent density of photoanodes, the photocurrent density of photoanodes was also tested with an Ag mirror under the same conditions. The detailed setup and results for the photoanodes with different mirrors are shown in Fig. S9. As seen in Fig. S9(c), the photocurrent density of TiO_2 with BS1 is higher than that with the Ag mirror. The reason for this is that the solar spectrum between 300 and 400 nm is absorbed significantly by the Ag mirror as shown in Fig. S10, which reduces the efficient utilization of solar energy by the TiO_2 photoanode.

Figure S9(d) shows that the photocurrent density of $BiVO_4$ with the Ag mirror is the highest among the four mirrors (Ag mirror, BS1 mirror, BS2 mirror, and BS1 + BS2 mirror). This is because the Ag mirror reflects a wider spectrum than BS1 and BS2. Although BS2 reflects only 420–480 nm spectrum to the $BiVO_4$ photoelectrode, the photocurrent density of $BiVO_4$ remains relatively high, as seen when comparing the photocurrent densities of $BiVO_4$ with Ag (Ag-$BiVO_4$) and BS2-$BiVO_4$, or $BiVO_4$ with BS1 + Ag (BS1 + Ag-$BiVO_4$) and $BiVO_4$ with BS1+BS2 (BS1+BS2-$BiVO_4$). The reason is that the spectrum reflected by BS2 aligns well with the absorbance range of $BiVO_4$. However, the photocurrent density of BS1+Ag-$BiVO_4$ is smaller than that with BS2, indicating that the available spectrum for $BiVO_4$ is reflected by BS1. The lowest photocurrent density was observed with $BiVO_4$ using BS1 + BS2, as only the 460–480 nm spectrum is utilized.

3.2.2 Performance of TiO_2 (front) photoanode and $BiVO_4$ (behind) photoanode (TiO_2+$BiVO_4$)

Although the result in Fig. 7 shows that the photocurrent of the TiO_2 + $BiVO_4$ system is higher than that of TiO_2 and $BiVO_4$ when positioned behind the TiO_2 photoelectrode, it is still much lower than the photocurrent of the BS1-TiO_2||BS2-$BiVO_4$ system, as shown in Fig. 6. The primary reason for this discrepancy is that the photocurrent density of $BiVO_4$ decreases when it is positioned behind the TiO_2 photoelectrode, due to the limited light transmittance of the TiO_2 layer. As shown in Fig. 8, although the intensity of light transmitted through the TiO_2 is 139.23 W/m^2, only 48.3 W/m^2 (34.7%) is effectively absorbed by the $BiVO_4$. This indicates that the performance of the tandem PEC water splitting system is significantly affected by the light transmittance of the front photoelectrode.

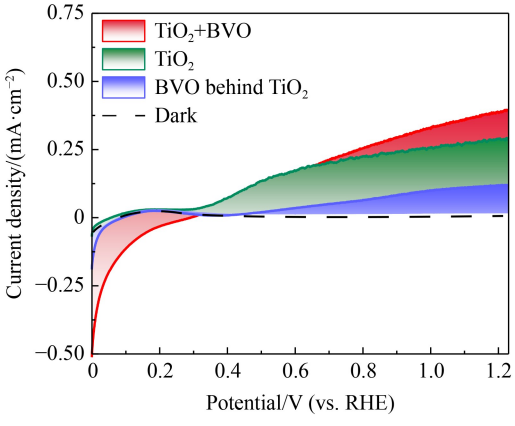

Fig. 7 Photocurrent density of TiO_2 + $BiVO_4$ in a three-electrode system.

The above results demonstrate that the photoelectrode can block solar light from reaching the photoanode or solar cell behind it, as its transmittance is much lower than that of the BSs. These BSs are typically prepared using high- and low-index materials alternatively, such as TiO_2 [42], Na_3AlF_6 [43], Si_3N_4 [44], Nb_2O_5 [45], and others.

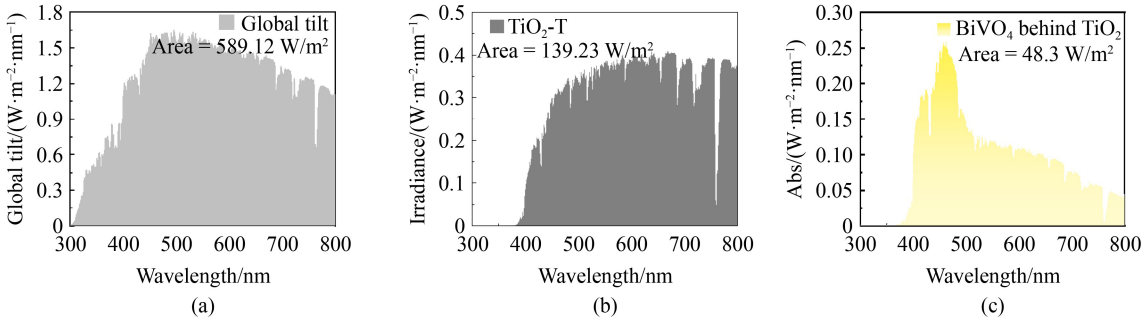

Fig. 8 Irradiance reaching to the photoelectrodes in the TiO_2 + $BiVO_4$ system.
(a) Overlap of AM 1.5 G solar spectrum (300–800 nm); (b) light spectrum of solar light after transmitting through TiO_2 electrode; (c) absorbance spectrum of $BiVO_4$ when placed behind TiO_2 electrode.

3.2.3 Performance of the TiO_2/$BiVO_4$

Figure 9 presents the photocurrent densities of the bare $BiVO_4$, bare TiO_2, and TiO_2/$BiVO_4$ photoanodes. The results show that the highest photocurrent density is generated by the $BiVO_4$ photoanode, reaching approximately 1 mA/cm² at 1.23 V versus RHE, rather than the TiO_2/$BiVO_4$. Despite the TiO_2/$BiVO_4$ electrode absorbing a broader range of the solar spectrum compared to both the TiO_2 and $BiVO_4$ electrodes, as shown in Fig. 10, its photocurrent density is lower than that of TiO_2 and $BiVO_4$. This suggests that other factors are indirectly affecting the performance of the TiO_2/$BiVO_4$ photoanode, which may include the contact resistance between the two layers, the alignment of the valence and conduction band edges, and the carrier transport kinetics, which could vary depending on the thickness of the films.

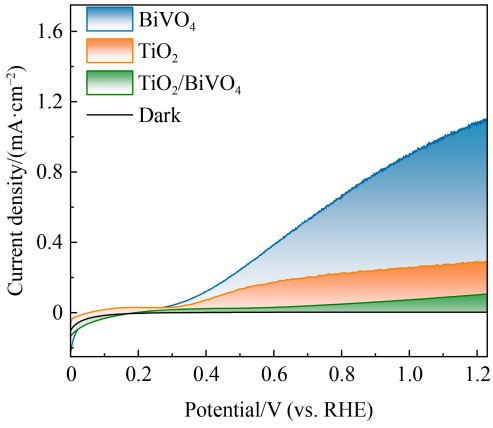

Fig. 9 Photocurrent density of TiO_2/$BiVO_4$ in a typical three-electrode system.

3.2.4 Comparation of different configuration of photoelectrodes

To investigate the behavior of different configurations of TiO_2 and $BiVO_4$, both with and without spectral BSs, their photocurrent densities were compared, as shown in Fig. 11. It should be emphasized that in Fig. 11, the hybrid photocurrent density of TiO_2(1)+BVO(2) should be divided by 2, as it is obtained by independently testing the BVO and TiO_2 under 1 sun intensity and then mathematically summing the values. The results reveal that the spectral BS significantly enhanced the photocurrent density of the multi-photoanode system, producing higher values than the TiO_2(1)+$BiVO_4$(2) configuration. In contrast, the photocurrent density of the TiO_2+$BiVO_4$ and TiO_2/$BiVO_4$ systems only reached 56.4% and 15.6%, respectively of the photocurrent density achieved by the TiO_2(1) + $BiVO_4$(2) setup. To

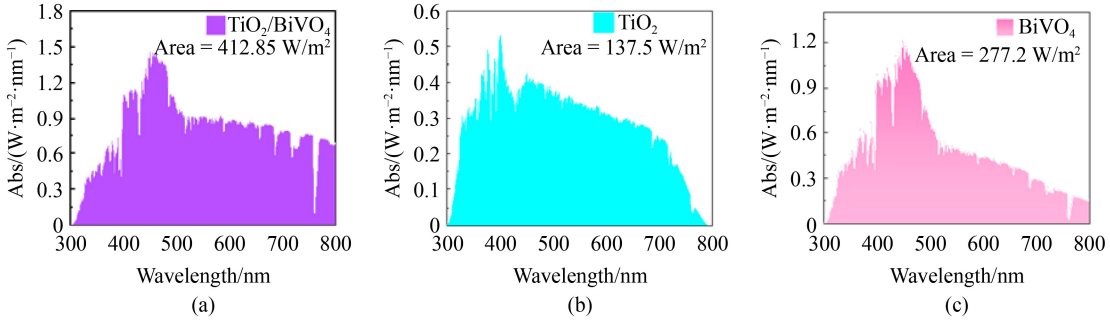

Fig. 10 Absorbance spectrum.
(a) TiO_2/$BiVO_4$; (b) TiO_2; (c) $BiVO_4$.

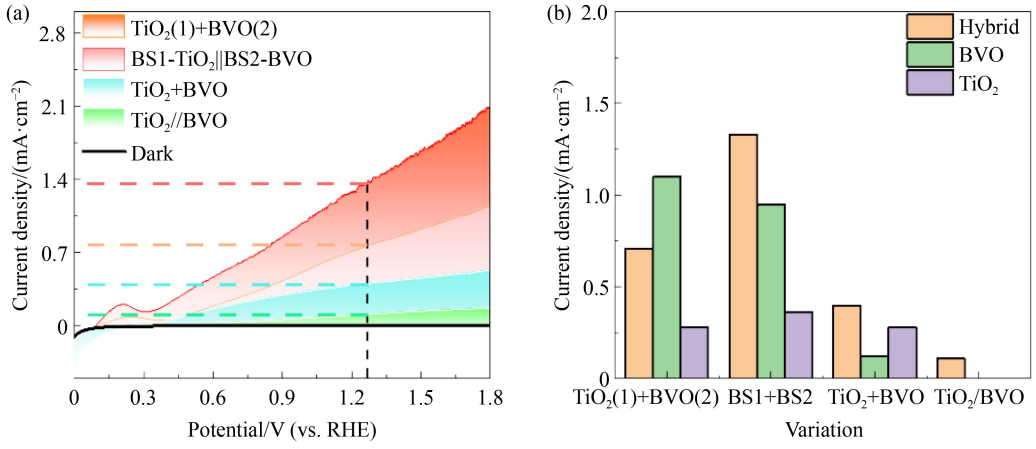

Fig. 11 Comparation of photocurrent densities of hybrid systems.
(a) Between potentials of 0–1.8 V versus RHE; (b) current contribution of hybrid and single TiO_2, $BiVO_4$ electrodes at 1.23 V versus RHE.

maximize the efficiency of self-biased PV-PEC water splitting, it is essential to simultaneously regulate both the current density of the PV cell and the photoelectrode.

3.3 Performance of different hybrid systems

The optimal arrangement of PV cells, photoanodes, and BSs is crucial for maximizing the performance of the hybrid PV-PEC system. To identify the most suitable module arrangement for the hybrid PV-PEC water splitting system, three different setups were experimentally investigated. Figure S11 shows the *I–V* curves of Si cells under various spectral fractionation conditions, with detailed performance parameters summarized in Tables S2–S4. For the BSs fractionation structure, the *I–V* curves of PV cells with BS2 and BS1 + BS2 fractionation were similar, as the transmission range of BS2 closely matches that of BS1 + BS2. Among the TiO_2 + $BiVO_4$ and TiO_2/$BiVO_4$ fractionation types, structures involving $BiVO_4$ photoanodes had a significantly greater impact on solar cells compared to those using only TiO_2 photoanodes. This is attributed to the broader absorption spectrum range of $BiVO_4$ photoanodes, as illustrated in Fig. S12. The *I–V* curves of PV cells and photoanodes are presented in Fig. 12, with data for the maximum power output and intersection points listed in Tables S5 and S6. As shown in Fig. 12, the intersection point of the *I–V* curves for the PV cell and photoanode is closer to the maximum power output of the PV cell when using two BSs, especially in the arrangement where two PV cells are connected in series. Additionally, the current density of the self-biased water splitting system comprising TiO_2 with BS1, $BiVO_4$ with BS2, and solar cell (BS1-TiO_2||BS2-BVO-PV) in Fig. 12(a) is approximately 1.71 and 2.7 times higher than the self-biased water splitting system of only $BiVO_4$ with BS2 and a solar cell (BS2-BVO-PV) and the self-biased water splitting system of TiO_2 with BS1 and a solar cell (BS1-TiO_2-PV), as shown in Figs. 12(b) and 12(c). This demonstrates the importance of selecting the appropriate arrangement for optimal system performance.

It is noteworthy that the current density of systems with two PV cells connected in series is higher than that of systems with a single PV cell, as shown in Figs. 12(d)–12(f). To maximize the efficiency of the PV-PEC system, the spectral BS should allocate as much of the spectrum as possible to match the absorbance of the photoanode in the PEC subsystem.

The comparison of current density and efficiency for various PV-PEC systems is shown in Fig. 13, with the corresponding the *I–t* curves provided in Fig. S13. The efficiency of the hybrid system with two BSs is higher than that of the system with a single BS, especially when the hybrid system includes two silicon cells. The current density in the BS1-TiO_2||BS2-BVO-PV system with two PV cells is approximately twice that in the BS1-TiO_2||BS2-BVO-PV system with a single PV cell. As shown in Fig. 13(b), the efficiency of BS2-BVO-PV and BS1-TiO_2-PV systems is approximately 85% and 15%, respectively, compared to the BS1-TiO_2||BS2-BVO-PV system with two PV cells connected in series. Therefore, optimizing the management of BSs will enhance the efficiency of PV-PEC water splitting.

The *I–V* curves of the PV cell and photoelectrodes for the other PV-PEC hybrid systems without a spectral BS is presented in Fig. 14, with detailed performance parameters listed in Table S7. It can be observed that the power output of Setup 3 (BS1-TiO_2||BS2-BVO-PV) with a single Si cell is 18.8 and 10.7 times higher than Setups 1 and 2, respectively. Notably, even though the voltages at the intersection points of the three hybrid systems do not change significantly, the differences in current densities are considerable. As depicted in Fig. S14, the current densities of Setups 1 and 2 are only 5.7% and 8.6% of Setup 3, respectively. It is also worth mentioning that the short-circuit current of the PV cell exceeds the

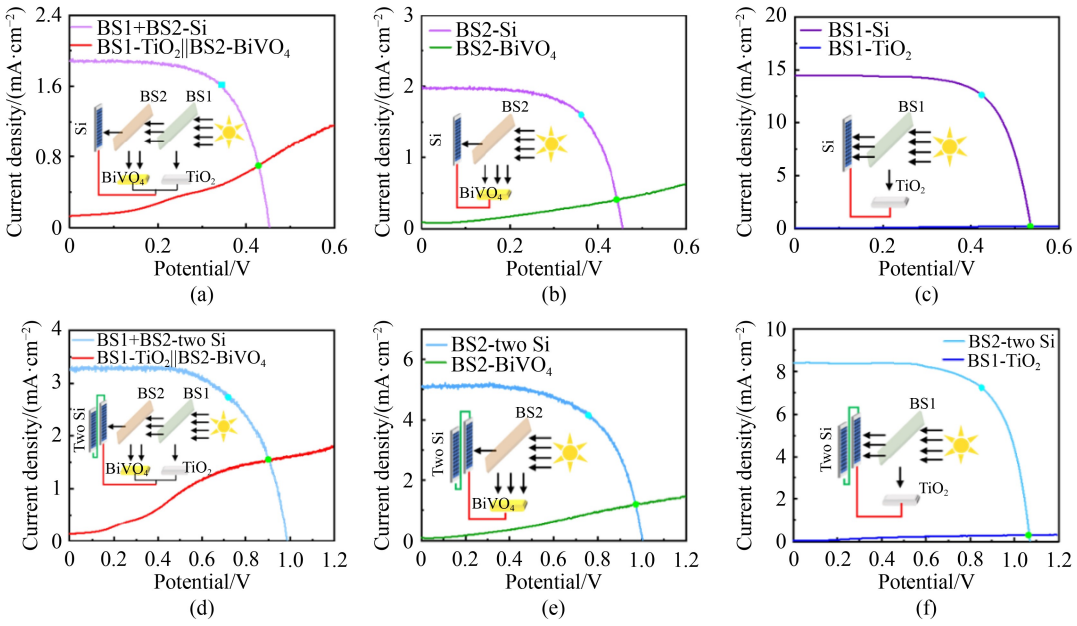

Fig. 12 *I–V* curves of PV cells and photoanodes.

(a, b, c) *I–V* curves of the single Si cell and TiO_2 + $BiVO_4$, $BiVO_4$, TiO_2 with BS1 + BS2, BS2, BS1, correspondingly; (d, e, f) *I–V* curves of two Si cells connected in series and photoanodes TiO_2 + $BiVO_4$, $BiVO_4$, TiO_2 with BS1 + BS2, BS2, BS1, correspondingly (the black straight line representing the light pathway, the red straight line representing the electricity pathway, and the green line representing two Si cells connected in series).

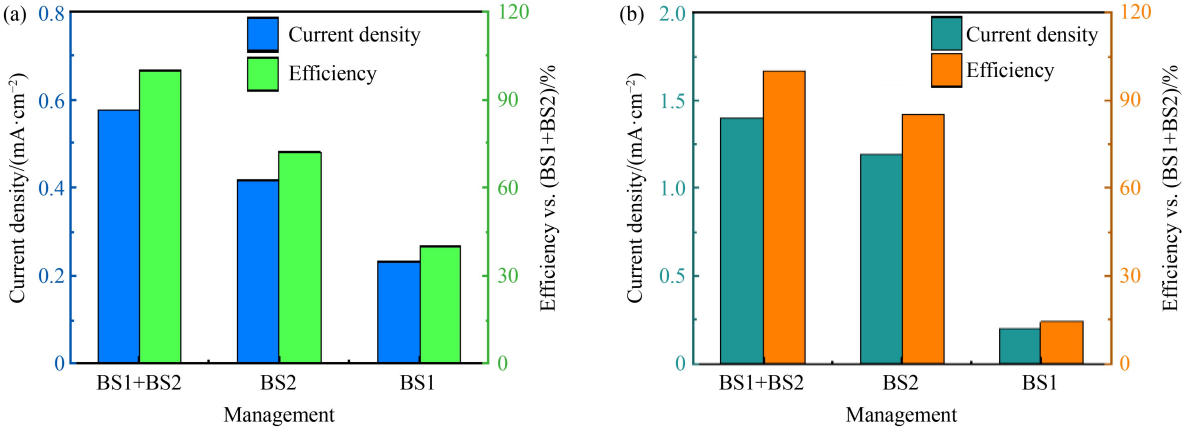

Fig. 13 Current density and efficiency of PV-PEC system.

(a) Using single Si cell; (b) using two Si cells connected in series as PV bias with spectral BSs.

photocurrent of photoelectrode, while the open-circuit voltage is insufficient for water splitting. This means that for an efficient PV-PEC water splitting system, a PV cell with a lager open-circuit voltage and a photoelectrode with higher photocurrent density are preferable.

To illustrate the practical application of the self-biased water splitting system with BSs, the STH efficiency of this structure in series with a single Si cell was compared with other recent representative reports (Table S8). Although the STH efficiency is lower than in other systems, it is still higher than that of the traditional structures (Setups 1 and 2). Considering the photocurrent density at the intersection point is 0.7 mA/cm^2 when the photoelectrodes are pure $BiVO_4$ and TiO_2, the STH conversion efficiency could increase further with optimization of the photoelectrodes.

To investigate the energy loss and utilization of each sub-component in the three hybrid systems, Sankey diagrams were plotted (Fig. 15) based on the UV-vis spectra of the BSs and photoanodes, with detailed calculations provided in Supplementary Notes 1 and 2. The reflection spectrum of different BSs and the transmittance spectrum of TiO_2+$BiVO_4$ and TiO_2/$BiVO_4$ arrangements are shown in Figs. S15 and S16. The

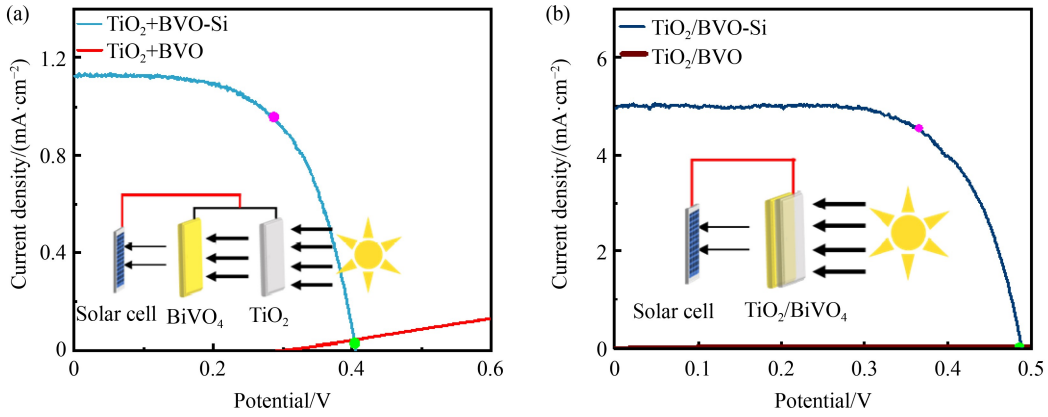

Fig. 14 *I–V* curves of two hybrid PV-PEC systems.
(a) *I–V* curves of Setup 1 (TiO_2 + BVO-PV); (b) *I–V* curves of Setup 2 (TiO_2/BVO-PV).

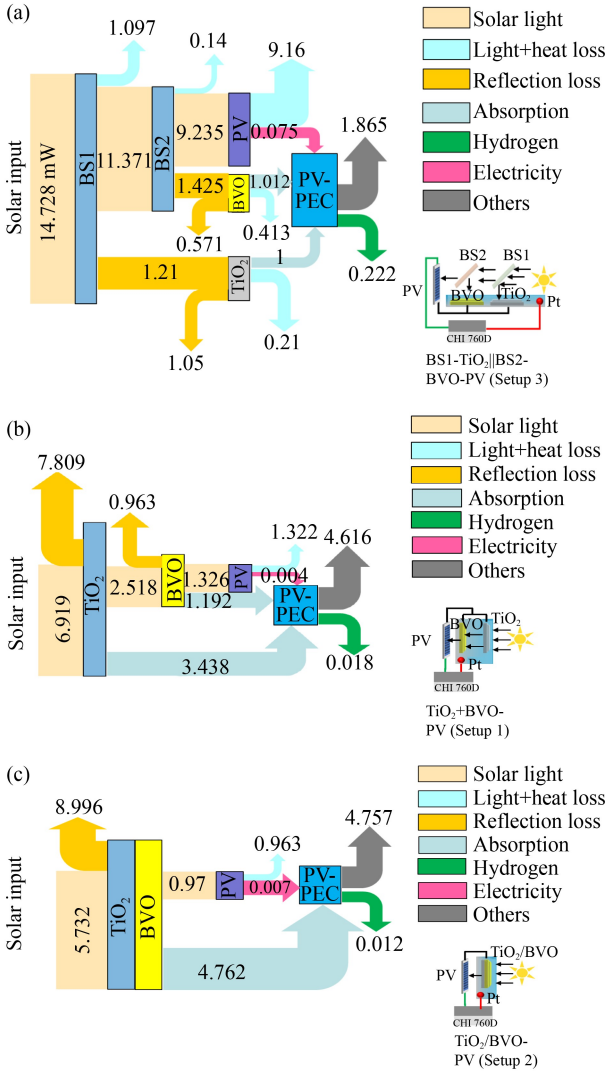

Fig. 15 Sankey diagrams showing magnitude and routing of energy flow.
(a) Through BS1-TiO_2||BS2-$BiVO_4$-PV; (b) TiO_2 + $BiVO_4$-PV, (c) TiO_2/$BiVO_4$-PV systems (the type of energy being denoted by the arrow colors).

electrical energy of the PV cell is calculated based on the data from Figs. 12 and 14.

Figure 15(a) shows the energy flow in the PV-PEC system with spectral BSs (Setup 3). For the BS1, approximately 77.2% of the solar energy transmitted through it to reaches the surface of BS2, with 19.5% reflected to the TiO_2 photoanode. The remaining 7.5% of solar energy is lost as heat dissipation due to light absorption by BS1. Approximately 81.2% of the transmitted solar energy reaching BS2 is further transmitted to the PV module, while only 17.6% of the energy are reflected to the $BiVO_4$ photoanode. The system with BSs produced 0.222 mW hydrogen energy, yielding a 1.5% STH efficiency. The light splitting performance of the BSs are already high over a wide spectral range, and further system efficiency improvements can be achieved by better matching the spectral range among the different components.

Figure 15(b) displays a similar energy flow calculation for the system without BSs (Setup 1). In this case, the solar energy reaching the TiO_2 and $BiVO_4$ photoanodes is greater than that in Setup 3. However, the STH of Setup 1 is only 0.122%, which is due to the low PEC conversion efficiency of the photoelectrodes. Compared to Setup 3, the hydrogen energy produced in Setup 1 is only 0.018 mW.

Figure 15(c) illustrated the energy flow for the TiO_2/$BiVO_4$ system (Setup 2), in which it can be seen that the hydrogen energy generated is lower than that from Setup 1. It should be noted that the reflection from the TiO_2/$BiVO_4$ photoanode is lower than that from Setup 1, while the absorbance is greater. The STH of Setup 2 is approximately 0.076%.

Figure S17(a) presents a quantitative comparison of the spectrum usage across three different setups. Although most of the solar energy is dissipated as the photothermal losses in the PV cell, the STH efficiency of Setup 3 is higher than that of Setups 1 and 2. Moreover, the light energy loss due to reflection from the photoelectrodes in

Setups 2 and 1 is larger than that in Setup 3. Figure S17(b) shows the specific quantities of the evolved O_2 and H_2 gases for Setup 3 over 150 min, with the H_2 and O_2 evolving in a stoichiometric ratio, and the H_2 generation rate approaching 12.1 μmol/(h·cm^2).

The above results demonstrate that an optimized arrangement of the PV cell and photoanodes with BSs can achieve higher performance than conventional tandem PV-PEC for water splitting. Moreover, the use of spectral BSs for accurately splitting the spectrum has been shown to be reliable, providing an innovative approach for self-biased water splitting. Furthermore, the more specific the spectrum range of the spectral BSs, the more effectively wavelengths can be assigned to each absorber, whether PV cell or photoelectrode, leading to enhanced overall performance in self-biased water splitting.

4 Conclusions

In this work, a PV-PEC water splitting system with BSs was designed and investigated, with a comparison to traditional tandem PV-PEC water splitting systems under simulated solar light illumination. In the PV-PEC water splitting system with BSs, incident light in different spectrum ranges is directed to TiO_2 and $BiVO_4$ photoelectrodes via reflection, while the transmitted light is utilized by the solar cell. The results show that solar energy utilization through spectrum splitting has a great effect on PEC water splitting, especially in systems with different light absorbers such as those with different photoelectrodes and solar cells.

Compared to the traditional Model T (Setups 1 and 2) PEC water splitting systems, the STH efficiency of the PV-PEC system with BSs (Setup 3) is 1.5%, representing a 12.38-fold and 19.87-fold enhancement over Setups 1 and 2, respectively. Furthermore, the current density of the photoelectrode in the system coupled with the BS does not experience a significant reduction, due to the higher optical efficiency of the BS compared to non-transparent photoelectrodes. The optimal current density of the self-biased water splitting system with BSs can reach 1.54 mA/cm^2 using two series-connected silicon cells. The experimental results show that the power output of the PV-PEC system with BSs (Setup 3) is 18.8 and 10.7 times greater than those of Setups 1 and 2, respectively.

If the solar energy absorbed by both the photoelectrodes and PV cells can be efficiently converted into hydrogen fuel or electricity, the performance of the overall water splitting system may be significantly enhanced. Further research should focus on developing high-performance photoelectrodes and optimizing the series-parallel configuration of PV cells for large-scale utilization of the integrated system. Additionally, it is crucial to study the coupling and energy redistribution principles between the different components of the integrated system to ensure optimal matching and maximize system-level efficiency.

Acknowledgements This work was supported by the National Key R&D Program of China (2021YFF0500504) and the Fundamental Research Funds for the Central Universities.

Competing Interests The authors declare that they have no competing interest.

Electronic Supplementary Material Supplementary material is available in the online version of this article at https://doi.org/10.1007/s11708-025-0984-6 and is accessible for authorized users.

Notations

BVO	$BiVO_4$ photoanode
BS	Beam splitter
BS1	Beam splitter which reflects 300–400 nm and transmits 460–800 nm
BS2	Beam splitter which reflects 420–480 nm and transmits 520–800 nmon of BS1
PV	Photovoltaic
PV-PEC	Photovoltaic-photoelectrochemical
STH	Solar-to-hydrogen
TiO_2(1)+BVO(2)	The sum of the current density of TiO_2 and $BiVO_4$ individually
TiO_2+BVO	TiO_2 (front) photoanode and $BiVO_4$ (behind) photoanode
TiO_2/BVO	Spin-coating $BiVO_4$ on TiO_2 photoanode
TiO_2/BVO-PV	PV cell behind the spin-coating $BiVO_4$ on TiO_2 photoanode
A	Area/cm^2
Abs	Absorbance/%
FF	Fill factor
I_{SC}	Short circuit current/mA
I_λ	Spectral irradiance/(W·m^{-2})
R	Reflection/%
T	Transmission/%
P_{light}	Solar input/(W·m^{-2})
P_{mpp}	Maximum power/mW
V_{OC}	Open circuit voltage/V
λ	Wavelength/nm
η	Efficiency/%

References

1. Zhao R, Yang W, Bu Q, Shi Y, Li Q, Yang L, Tang J. Peroxymonosulfate-assisted photocatalysis system enhanced

magnetic Fe_3O_4@P-C_3N_4 treatment of tetracycline wastewater: Multi-pathways mediated electrons migration to generate reactive species. Journal of Colloid and Interface Science, 2025, 678(PA): 987–1000
2. Suryawanshi M P, Ghorpade U V, Toe C Y, et al. Earth-abundant photoelectrodes for water splitting and alternate oxidation reactions: Recent advances and future perspectives. Progress in Materials Science, 2023, 134: 101073
3. Park H, Kim S, Kim T, et al. CoS@TiO_2 S-scheme heterojunction photocatalyst for hydrogen production from photoinduced water splitting. Journal of Cleaner Production, 2021, 319: 128819
4. Chen Y, Zheng W, Murcia-López S, et al. Light management in photoelectrochemical water splitting—From materials to device engineering. Journal of Materials Chemistry. C, Materials for Optical and Electronic Devices, 2021, 9(11): 3726–3748
5. Wang Q, Pornrungroj C, Linley S, et al. Strategies to improve light utilization in solar fuel synthesis. Nature Energy, 2021, 7(1): 13–24
6. Wang B, Yang S, Zhang T, et al. Analysis of an electrolyte's pH-dependent performance during solar water splitting. Industrial & Engineering Chemistry Research, 2023, 62(38): 15406–15417
7. Wang B, Yang S, Lai Y, et al. Enhanced photoelectrochemical water splitting via 3D flow field structure: Unveiling the decisive role of interfacial mass transfer. Chemical Engineering Research & Design, 2024, 205: 268–279
8. Shi X, Jeong H, Oh S J, et al. Unassisted photoelectrochemical water splitting exceeding 7% solar-to-hydrogen conversion efficiency using photon recycling. Nature Communications, 2016, 7(1): 11943
9. Gong Z, Liu B, Zhang P, et al. Performance prediction of multiple photoanodes systems for unbiased photoelectrochemical water splitting. ACS Materials Letters, 2021, 3(7): 939–946
10. Liang Q, Huang Y, Guo Y, et al. Efficient osmosis-powered production of green hydrogen. Nature Sustainability, 2024, 7: 628–639
11. Jiang F, Gunawan, Harada T, et al. Pt/In_2S_3/CdS/Cu_2ZnSnS_4 thin film as an efficient and stable photocathode for water reduction under sunlight radiation. Journal of the American Chemical Society, 2015, 137(42): 13691–13697
12. Ding C, Qin W, Wang N, et al. Solar-to-hydrogen efficiency exceeding 2.5% achieved for overall water splitting with an all earth-abundant dual-photoelectrode. Physical Chemistry Chemical Physics, 2014, 16(29): 15608–15614
13. AlOtaibi B, Fan S, Vanka S, et al. A metal-nitride nanowire dual-photoelectrode device for unassisted solar-to-hydrogen conversion under parallel illumination. Nano Letters, 2015, 15(10): 6821–6828
14. Fan R, Cheng S, Huang G, et al. Unassisted solar water splitting with 9.8% efficiency and over 100 h stability based on Si solar cells and photoelectrodes catalyzed by bifunctional Ni–Mo/Ni. Journal of Materials Chemistry. A, Materials for Energy and Sustainability, 2019, 7(5): 2200–2209
15. Ma Z, Ma X, Yang L, et al. Novel K-doped TiO_2 nanotube arrays with superhydrophilic surface and high photoelectrochemical cathodic protection. Applied Surface Science, 2022, 580: 152274
16. Fernández-Domene R M, Sánchez-Tovar R, Sánchez-González S, et al. Photoelectrochemical characterization of anatase-rutile mixed TiO_2 nanosponges. International Journal of Hydrogen Energy, 2016, 41(41): 380–388
17. Yuan J, Li C, Li T, et al. Remarkably promoted photoelectrochemical water oxidation on TiO_2 nanowire arrays via polymer-mediated self-assembly of CoO_x nanoparticles. Solar Energy Materials and Solar Cells, 2020, 207: 110349
18. Dong C, Yang Y, Hu X, et al. Self-cycled photo-Fenton-like system based on an artificial leaf with a solar-to-H_2O_2 conversion efficiency of 1.46%. Nature Communications, 2022, 13(1): 4982
19. Li Y, Mei Q, Liu Z, et al. Fluorine-doped iron oxyhydroxide cocatalyst: promotion on the WO_3 photoanode conducted photoelectrochemical water splitting. Applied Catalysis B: Environmental, 2022, 304: 120995
20. Lee M G, Yang J W, Park I J, et al. Tailored $BiVO_4$/In_2O_3 nanostructures with boosted charge separation ability toward unassisted water splitting. Carbon Energy, 2023, 5(6): e321
21. Liang X, Wang P, Tong F, et al. Bias-free solar water splitting by tetragonal zircon $BiVO_4$ nanocrystal photocathode and monoclinic scheelite $BiVO_4$ nanoporous photoanode. Advanced Functional Materials, 2021, 31(8): 2008656
22. Brillet J, Yum J H, Cornuz M, et al. Highly efficient water splitting by a dual-absorber tandem cell. Nature Photonics, 2012, 6(12): 824–828
23. Li C, Ma S, Zhao M, et al. Self-Assembled α-Fe_2O_3@Co_3O_4/graphene quantum dot core-hybrid shell wormlike nanoarrays with synergistic effects for photoelectrochemical water oxidation. ACS Sustainable Chemistry & Engineering, 2023, 11(32): 102–113
24. Wang S, Chen P, Bai Y, et al. New $BiVO_4$ dual photoanodes with enriched oxygen vacancies for efficient solar-driven water splitting. Advanced Materials, 2018, 30(20): 1800486
25. Huang G, Markides C N. Spectral-splitting hybrid PV-thermal (PV-T) solar collectors employing semi-transparent solar cells as optical filters. Energy Conversion and Management, 2021, 248: 114776
26. Zhu T, Li Q, Yu A. Analysis of the solar spectrum allocation in a spectral-splitting photovoltaic-thermochemical hybrid system. Solar Energy, 2022, 232: 63–72
27. Liang H, Wang F, Yang L, et al. Progress in full spectrum solar energy utilization by spectral beam splitting hybrid PV/T system. Renewable & Sustainable Energy Reviews, 2021, 141: 110785
28. Bicer Y, Dincer I. Experimental investigation of a PV-coupled photoelectrochemical hydrogen production system. International Journal of Hydrogen Energy, 2017, 42(4): 2512–2521
29. Lee J W, Song M S, Jung H S, et al. Development of solar radiation spectrum-controlled emulsion filter for a photovoltaic-thermal (PVT) system. Energy Conversion and Management, 2023, 287: 117087
30. Cui T, Xuan Y, Li Q. Design of a novel concentrating photovoltaic–thermoelectric system incorporated with phase change materials. Energy Conversion and Management, 2016, 112: 49–60
31. Kandil A A, Salem M S, Awad M M, et al. Adaptation of the solar spectrum to improve the use of sunlight: A critical review on techniques, applications, and current trends. Advanced

Sustainable Systems, 2023, 7(6): 2300012
32. Wingert R, O'Hern H, Orosz M, et al. Spectral beam splitting retrofit for hybrid PV/T using existing parabolic trough power plants for enhanced power output. Solar Energy, 2020, 202: 1–9
33. Wang G, Yao Y, Lin J, et al. Design and thermodynamic analysis of a novel solar CPV and thermal combined system utilizing spectral beam splitter. Renewable Energy, 2020, 155: 1091–1102
34. Yazdanifard F, Ameri M, Taylor R A. Numerical modeling of a concentrated photovoltaic/thermal system which utilizes a PCM and nanofluid spectral splitting. Energy Conversion and Management, 2020, 215: 112927
35. Huaxu L, Fuqiang W, Dong Z, et al. Experimental investigation of cost-effective ZnO nanofluid based spectral splitting CPV/T system. Energy, 2020, 194: 116913
36. Lu K, Yu Q, Zhao B, et al. Performance analysis of a novel PV/T hybrid system based on spectral beam splitting. Renewable Energy, 2023, 207: 398–406
37. Kandil A A, Awad M M, Sultan G I, et al. Performance of a photovoltaic/thermoelectric generator hybrid system with a beam splitter under maximum permissible operating conditions. Energy Conversion and Management, 2023, 280: 116795
38. Wu H, Zhou Z, Shan S. Optimal design principle of a cascading solar photovoltaic system with concentrating spectrum splitting and reshaping. Renewable Energy, 2022, 197: 197–210
39. Hogerwaard J, Dincer I, Naterer G F. Experimental investigation and optimization of integrated photovoltaic and photoelectrochemical hydrogen generation. Energy Conversion and Management, 2020, 207: 112541
40. Yang S, Wang B, Zhao R, et al. Enhanced photoelectrochemical performance of NiS-modified TiO_2 nanorods with a surface charge accumulation facet. Dalton Transactions, 2023, 52(44): 16442–16450
41. Yang N, Zhang S, Xiao Y, et al. Insight into the key restriction of $BiVO_4$ photoanodes prepared by pyrolysis method for scalable preparation. Angewandte Chemie International Edition, 2023, 62(39): e202308729
42. Kim D, Kim K M, Han H, et al. $Ti/TiO_2/SiO_2$ multilayer thin films with enhanced spectral selectivity for optical narrow bandpass filters. Scientific Reports, 2022, 12(1): 1–10
43. Li J, Yang Z, Ge Y, et al. Performance study of photovoltaic-thermochemical hybrid system with Cassegrain concentrator and spectral splitting integration. Energy, 2024, 292: 130611
44. Mahmoudinezhad S, Cotfas D T, Cotfas P A, et al. Experimental investigation on spectrum beam splitting photovoltaic–thermoelectric generator under moderate solar concentrations. Energy, 2022, 238: 121988
45. Agabekov V E, Kazak N S, Belyi V N, et al. Broad-band polarizing light beam splitter based on a multilayer thin-film coating. Journal of Applied Spectroscopy, 2021, 88(4): 816–824